ACS NANO

www.acsnano.org

ARTICLE

Ultrastable Dendrite-Free Potassium Metal Batteries Enabled by Weakly-Solvated Electrolyte

Ping Gao,[‖] Fei Zhang,[‖] Xingchao Wang,* Miaomiao Wu, Qian Xiang, Aikai Yang,* Ying Sun,* Jixi Guo, and Yudai Huang

Cite This: *ACS Nano* 2023, 17, 20325−20333

Read Online

ACCESS | Metrics & More | Article Recommendations | Supporting Information

ABSTRACT: **Potassium (K) metal is considered one of the most promising anodes for potassium metal batteries (PMBs) because of its abundant and low-cost advantages but suffers from serious dendritic growth and parasitic reactions, resulting in poor cyclability, low Coulombic efficiency (CE), and safety concerns. In this work, we report a localized high-concentration electrolyte (LHCE) consisting of potassium bis(fluorosulfonyl)imide (KFSI) in a cosolvent of 1,2-dimethoxyethane (DME) and 1,1,2,2,2-tetrafluoroethyl-2,2,3,3-tetrafluoropropyl ether (TTE) to solve the problems of PMBs. TTE as a diluent not only endows LHCE with advantages of low viscosity, good wettability, and improved conductivity but also solves the dendrite problem pertaining to K metal anodes. Using the formulation of LHCE, a CE of 98% during 800 cycles in the K||Cu cell and extremely stable cycling of over 2000 h in the K||K symmetric cell are achieved at a current density of 0.1 mA cm^{-2}. In addition, the LHCE shows good compatibility with a Prussian Blue cathode, allowing almost 99% CE for the K||KFe^{II}Fe^{III}(CN)$_6$ full cell during 100 cycles. This promising electrolyte design realizes high-safety and energy-dense PMBs.**

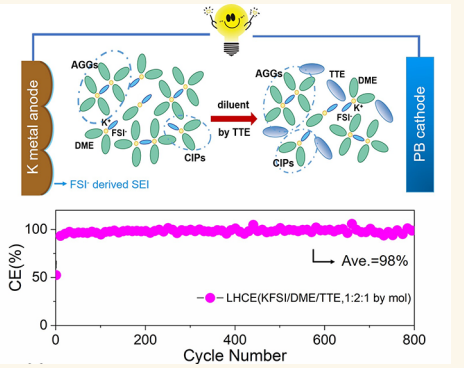

KEYWORDS: *PMBs, localized high-concentration electrolyte, SEI, dendrite-free, long cycle life*

Lithium-ion batteries (LIBs) have gained significant popularity as a prominent rechargeable energy storage solution for portable electronic devices owing to their high energy density.[1−6] Nevertheless, apprehensions regarding the limited availability, unequal distribution, and exorbitant cost of lithium have prompted the scientific community to contemplate sustainable supply options and explore alternative rechargeable battery technologies.[7−13] More recently, potassium metal batteries (PMBs) are considered a promising alternative to LIBs due to the great abundance and low cost of potassium anodes.[14−19] Yet, the deployment of K metal anodes is hampered severely by dendrites and a limited Coulombic efficiency (CE) during repeated plating/stripping. During cycling, K^+ is typically deposited in dendritic form on K metal surface due to inhomogeneous current distribution and cation concentration gradients in the traditional electrolyte, as well as the fracture of the solid electrolyte interface (SEI),[20−22] leading to an internal short circuit and thermal runaway accidents.[23,24] On the other hand, the use of a fresh K metal anode with a commercial electrolyte induces continuous formation of an SEI and depletion of electrolyte, which ultimately results in poor CE and severe battery capacity degradation. Therefore, the practical application of PMBs relies heavily on finding solutions to problems related to K metal anodes.

Several solutions to address the problems of K anodes involve optimizing electrolyte compositions,[25] fabricating multifunctional separators,[18,26] and designing various composite K metal anodes.[18,27−33] Recently, concentrated electrolytes, particularly high-concentration electrolytes (HCEs), have emerged as a promising strategy to stabilize the K anode. HCEs with high salt-to-solvent molar ratios reduce the number of free solvent molecules while improving the stability of the interfacial chemistry between the electrolyte and the anode. Nonetheless, the HCEs suffer from several disadvantages with respect to high viscosity, poor wettability, and high cost, which limit their practical application. Numerous types of solvents are added to HCEs as diluents to form localized high-

Received: July 12, 2023
Accepted: October 11, 2023
Published: October 13, 2023

https://doi.org/10.1021/acsnano.3c06368
ACS Nano 2023, 17, 20325−20333

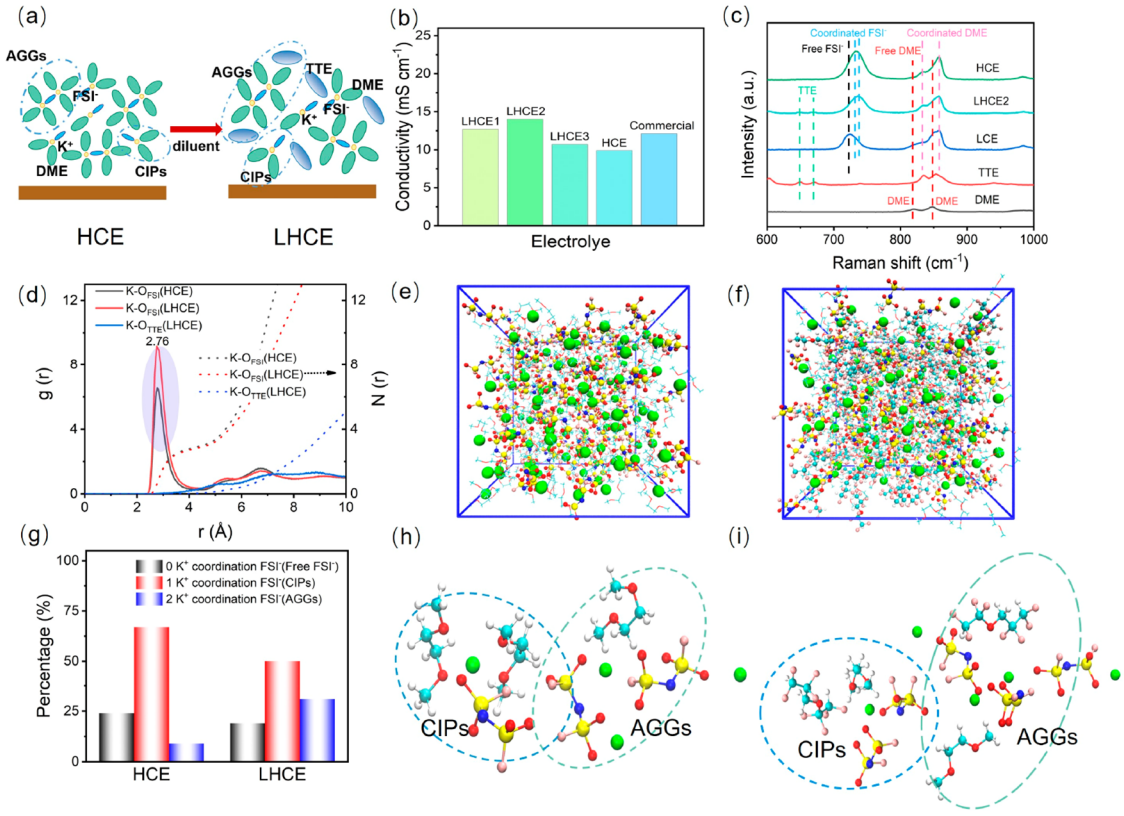

Figure 1. (a) Dilution schematic from the HCE to the LHCE. (b) Ionic conductivity and (c) Raman spectra of different electrolytes. (d) RDFs (solid lines) and coordination numbers (dashed lines) and (g) the coordination ratios of HCE and LHCE. Simulated snapshots of (e) HCE and (f) LHCE2. Extraction of the main K^+ coordination structures in (h) HCE and (i) LHCE2 from the MD simulation snapshots. Atom colors: K, green; O, red; N, blue; S, yellow; F, pink; C, cyan; H, white.

concentration electrolytes (LHCEs) to overcome the inherent drawbacks of HCEs. Diluents are used as inert additives in electrolytes to reduce the salt concentration and viscosity. These additives do not alter the inherent solvation structure of the electrolyte but significantly increase the ionic conductivity and improve the electrolyte wettability of the electrolyte.[2,24,34−37] For example, fluorinated ethers are the most commonly used diluents for HCEs in lithium metal batteries (LMBs) and sodium metal batteries (SMBs) by virtue of a high dielectric constant and low donor number.[38] Zhang et al. introduced bis(2,2,2-trifluoroethyl) ether as a multifunctional diluent to high-concentration lithium difluorosulfonimide (LiFSI)/dimethyl carbonate (DMC) for LMBs and sodium difluorosulfonimide (NaFSI)/1,2-dimethoxyethane (DME) for SMBs.[39] Wang et al. successfully created dendrite-free LMBs by diluting concentrated LiFSI/DMC with 1,1,2,2,2-tetrafluoroethyl-2,2,3,3-tetrafluoropropyl ether (TTE), which exhibited stable cycling performance.[40,41] Inspired by the concept of LHCEs widely used in LMBs and SMBs, we were inspired by whether these strategies could address the challenges faced by PMBs. However, as far as we know, there are currently few reports on LHCEs for PMBs.

Herein, we elaborate a type of LHCE for PMBs using KFSI as the salt, DME as the solvent, and TTE as a diluent. The LHCE was found to inhibit dendrite growth and improve CE due to the enhanced binding strength between K^+ cations and FSI^- anions, which promoted the preferential reduction of more FSI^- anions to generate a KF-rich SEI on the K anode surface. The electrolyte also had high ionic conductivity and good wettability. Consequently, the combined merits of LHCE enabled dendrite-free K deposition with an average CE of >98% through 800 cycles in a K||Cu cell and an ultralong cycling life of more than 1000 cycles (i.e., over 2000 h) at a current density of 0.1 mA cm^{-2} in a K||K symmetric cell. In addition, the K||$KFe^{II}Fe^{III}(CN)_6$ full cell equipped with LHCE delivered a reversible capacity of 67 mAh g^{-1} with good cycling stability.

RESULTS AND DISCUSSION

TTE was selected as a diluent in this study and added directly to KFSI/DME to form the LHCE (Figure 1a). To optimize the addition of TTE, three types of LHCEs (LHCE1, KFSI/DME/TTE = 1:2:0.5; LHCE2, KFSI/DME/TTE = 1:2:1; LHCE3. KFSI/DME/TTE = 1:2:1.5, by mol) were prepared (Figure S1a). After a 24 h rest, some salt precipitated from LHCE3 (Figure S1b), possibly due to the addition of excess TTE. Figure 1b displays the ionic conductivity of three LHCEs, revealing that LHCE2 has the highest ionic conductivity (14.0 mS cm^{-1}), followed by LHCE1 (12.7 mS cm^{-1}), LHCE3 (10.7 mS cm^{-1}), and HCE (KFSI/DME = 1:2) (9.9 mS cm^{-1}). This illustrates that the ionic conductivity of the electrolyte is significantly improved by the low viscosity of TTE. The ionic conductivity of LHCEs is expected to increase gradually with increasing TTE; however, in the case of LHCE3, the ionic conductivity decreases. This is likely due to the supersaturation of the solution resulting from the excessive addition of TTE to LHCE3. The wetting behavior of various electrolytes on a polypropylene (PP) separator was characterized (Figures S2 and S3). The results showed that the HCE did not wet the surface of the PP separator even after 30 s,

https://doi.org/10.1021/acsnano.3c06368
ACS Nano 2023, 17, 20325−20333

whereas LHCEs exhibited good wettability as they immediately and completely penetrated and immersed the separator. Additionally, the contact angles of LHCE1, LHCE2, and LHCE3 on PP separators were 35.3, 24.6, and 50.8°, respectively, which were significantly smaller than that of HCE (θ_{CA} = 52.5°). These findings suggest that LHCEs have good wettability and contribute to a lower interfacial resistance for K^+ transference. In addition, the superior electrochemical stability of LHCE2 was investigated by linear scanning voltammetry (LSV). As shown in Figure S4, the electrochemical window of LHCE2 (4.3 V vs K^+/K) is slightly higher than that of the HCE (4.2 V vs K^+/K) and significantly wider than that of the low concentration electrolyte (LCE) (3.5 V vs K^+/K), greatly broadening the choice of electrode materials.

The effect of TTE on the solvation structure in electrolytes was investigated by Raman spectroscopy (Figure 1c). In pure DME, the signals at Raman shifts of 820 and 847 cm^{-1} (red) were identified as the $-CH_2-O-CH_3$ stretching vibrations of free DME molecules. In LCE, the characteristic peaks of free DME molecules decreased, while new peaks appeared at 832 and 857 cm^{-1} (pink), corresponding to the coordinated DME molecules. The peak at 724 cm^{-1} (black line) was attributed to free FSI^- anions in the electrolyte. In HCE, the characteristic peaks of free DME molecules and FSI^- anions vanished and a new peak at 735 cm^{-1} (blue) was observed, representing the solvated FSI^- anions. The characteristic peaks of TTE in LHCE2 corresponding to the vibrational band were observed at 650 and 669 cm^{-1} (green line), indicating that TTE does not play a role in the solvation structure. Notably, the coordinated FSI^- peak shifted from 735 to 737 cm^{-1}, implying enhanced coordination between K^+ cations and FSI^- anions after the addition of TTE.[40]

MD simulations were conducted to validate the impact of TTE on LHCE2 and HCE. Figure 1d illustrates the radial distribution functions (RDFs) of LHCE2 and HCE. The peak of LHCE2 at 2.76 Å corresponds to the $K-O_{FSI^-}$ coordination structure, which is larger than that of HCE, indicating the enhanced coordination of K^+-FSI^-. Notably, LHCE2 did not show any significant peak of $K-O_{TTE}$, indicating a weak or negligible solvated TTE with K^+. Furthermore, an MD simulation unveils the changes in the content of contact ion pairs (CIPs, FSI^- coordinated to one K^+) and aggregated ion pairs (AGGs, FSI^- coordinated to two or more K^+). As shown in Figure 1e–i, the AGG ratio of LHCE2 was higher than that of HCE, further verifying the enhanced coordination of K^+-FSI^- caused by TTE addition, which is consistent with the findings of the Raman spectra. By virtue of the well-maintained solvation structure of K^+-FSI^-–DME, LHCE2 was anticipated to exhibit distinctive characteristics resembling HCE with regard to stabilizing K metal anodes while simultaneously maintaining a low-viscosity behavior.

To assess the ability of LHCEs to suppress the growth of dendrites, K||Cu cells were constructed using different electrolytes. As shown in Figure 2a, the K||Cu cell employing LHCE2 demonstrated a significantly higher CE (98.1%) compared to those with HCE (95.5%), LCE (89.2%), and commercial electrolyte (57.1%). This superior performance of LHCE2 is attributed to its ability to effectively suppress K dendrite growth and promote uniform K deposition. It is worth noting that although HCE had fewer free solvent molecules and exhibited an improved CE compared to the commercial electrolyte and LCE, its high viscosity resulted in lower ionic conductivity and poorer wettability, ultimately leading to an

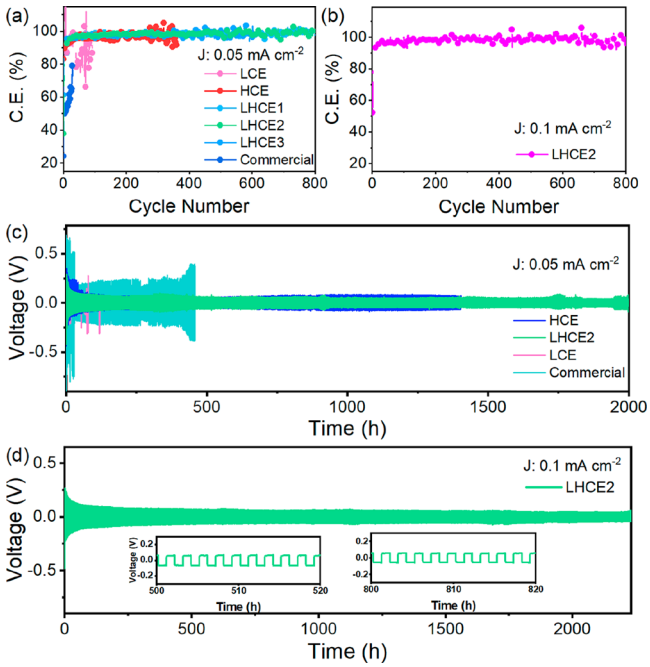

Figure 2. (a) Comparison of K plating/stripping on the Cu electrode in different electrolytes at a current of 0.05 mA cm^{-2} with an areal capacity of 0.05 mAh cm^{-2} and (b) cycling performance with LHCE at a current of 0.1 mA cm^{-2} with an areal capacity of 0.1 mAh cm^{-2}. Long cycling performance of K||K cells using (c) different electrolytes at a current of 0.05 mA cm^{-2} with an areal capacity of 0.05 mAh cm^{-2} and (d) LHCE at a current of 0.1 mA cm^{-2} with an areal capacity of 0.1 mAh cm^{-2}. Magnified voltage profiles at different stages of cycling at the current of 0.1 mA cm^{-2} with an areal capacity of 0.1 mAh cm^{-2} are shown as insets in (d).

inferior cycling performance. The lower CE observed in K||Cu cells using commercial electrolyte and LCE can be ascribed to irreversible side reactions between the deposited K metal and the electrolytes, inevitably resulting in a significant reduction in capacity and reversibility.[19,28] In addition, even at a higher current density of 0.1 mA cm^{-2} and an areal capacity of 0.1 mAh cm^{-2}, the K||Cu cell equipped with LHCE2 demonstrated excellent reversible K plating/stripping behavior, achieving an average CE of 98% over 800 cycles (Figure 2b).

The superiority of LHCEs was further verified by the plating/stripping curves of the K||Cu cells. The overpotential of a K||Cu cell using LHCE2 was significantly lower (202 mV) than those using the other two LHCEs (224 and 288 mV), HCE (222 mV), and commercial electrolyte (256 mV) (Figure S5). It is worth noting that, although K||Cu cells using LCE displayed a lower overpotential compared to those using LHCE2, they suffered from poor cycle stability caused by severe irreversible side reactions. On the other hand, K||Cu cells assembled with LHCE2 exhibited ultralong cycling stability of over 350 cycles with a limited increase of polarization, demonstrating the excellent reversible chemical behavior of K plating/stripping (Figure S6). This is the best cycling performance report to date for K||Cu cells (Table S1). These findings suggest that the addition of TTE to LHCE effectively addresses the issues associated with the K metal anode of PMBs.

The stability and long-term compatibility of various electrolytes with K metal anodes were investigated by using

https://doi.org/10.1021/acsnano.3c06368
ACS Nano 2023, 17, 20325–20333

K||K cells. The test conditions were a current density of 0.05 mA cm^{-2} and a deposition capacity of 0.05 mAh cm^{-2}. The commercial electrolyte used in K||K cells exhibited a large polarization voltage (>200 mV) and voltage fluctuation during cycling due to poor interfacial stability with the K metal anode (Figure 2c). The LCE cells also displayed an unstable polarization voltage with significant fluctuations, resulting in short circuits after 80 h of cycling. In contrast, the HCE cells exhibited stable cycling of K-metal plating/stripping due to the inhibitory effect of the KFSI salt on K dendrites,[42,43] but with a higher interfacial resistance that led to larger polarization voltage. The K||K cells using LHCE2 had extremely stable cycling for 2000 h (~1000 successive plating/stripping cycles) with a low polarization voltage of <50 mV, significantly outperforming other electrolytes.

Especially, an overwhelming cycling stability of over 2000 h with an extremely stable voltage distribution (<60 mV) can be obtained even at a higher current density of 0.1 mA cm^{-2} with a higher areal capacity of 0.1 mAh cm^{-2} (Figure 2d). Moreover, the voltage fluctuations of K||K cells with LHCE2 were significantly smaller than those with LHCE1 and LHCE3 at various current densities (Figure S7). The cycling performance of K||K cells using LHCE2 was also much better than those using LHCE1 and LHCE3. These results were mainly attributed to the superior interface compatibility and wettability of LHCE2, proving its feasibility in achieving long-life PMBs.

Scanning electron microscopy (SEM) was used to examine the morphology of K deposited on Cu electrodes after cycling in various electrolytes. The commercial electrolyte resulted in nonuniform K deposition, leading to dendrite growth and potential puncture of the separator, ultimately causing short-circuiting of the cell (Figure 3a). In contrast, nodular K

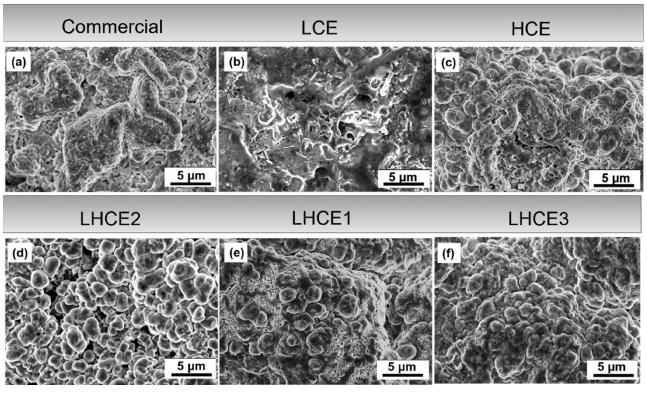

Figure 3. SEM images of Cu electrodes with K deposited at a current of 0.1 mA cm^{-2} with an areal capacity of 0.1 mAh cm^{-2} in different types of electrolytes: (a) Commercial; (b) LCE; (c) HCE; (d) LHCE2; (e) LHCE1; (f) LHCE3.

deposits with a particle size of 0.5−1 μm were observed in LCE (Figure 3b). However, smaller particles had larger contact areas with the electrolyte, leading to severe side reactions and a lower CE. The K metal surface deposited in HCE exhibited a homogeneous nodular structure, which is less likely to puncture separators (Figure 3c). Additionally, the K metal surfaces deposited on Cu electrodes in LHCE2 were uniformly covered with many nodular K deposits, exhibiting a flat and uniform morphology, with each region consisting of many tiny crystals (Figure 3d). This ordered interface behavior facilitates the formation of a dense SEI layer and prevents excessive parasitic reactions, thereby keeping dendrite-free K metal during cycling. Compared to HCE, LHCE1, and LHCE3, the K metal surface deposited in LHCE2 was more uniformly flat (Figure 3c,e,f), leading to more stable cycling and higher CE. The SEI formed in LHCE2 (Figure S8) was composed of C, O, F, S, and K elements, as demonstrated by EDS analysis, and was uniformly distributed on the electrode surface, contributing to homogeneous K deposition.

To reveal the mechanism of SEI formation and stable K plating/stripping behavior, K anodes after being cycled in different electrolytes were investigated by X-ray photoelectron spectroscopy (XPS) with an argon ion etching technique (Figure 4 and Figure S9). Clearly, the K metal surfaces show a great number of decomposition products, including RO−, K_2CO_3, KF, and C−K/C−C/C−H/C−O. These products can create an SEI layer on the surface of K metal, where inorganic species like KF and S═O bonds play a key role in inducing homogeneous K deposition. The SEI layer formed in HCE and LHCE contains higher contents of KF and S═O bonds compared to commercial electrolyte. In LHCE, KF is the main reduction product of KFSI, which can be attributed to the fact that KFSI with a lower LUMO (the lowest unoccupied molecular orbital) (−0.86 eV) decomposes first before TTE (1.04 eV) (Figure 5a,b).[40,44]

Figure 5c−f provides a detailed illustration of the K^+ solvation structures and SEI formation mechanisms in different electrolytes. In the commercial electrolyte, K^+ is solvated by a large amount of carbonate solvent and a small amount of PF_6^- anions. The solvated K^+ then moves toward the K anode, where the carbonate solvent molecules and a small proportion of PF_6^- anions are reduced to form an organic-rich SEI layer.[40,45−47] The SEI layer in LCE mainly originates from the breakdown of the solvent DME and a small amount of free FSI^- anions.[45] In contrast, the HCE and the LHCE contain more solvated FSI^-, which are reduced on the K metal surface to form an inorganically enriched SEI. This SEI inhibits K dendrite growth and promotes highly homogeneous K deposition.[7,40,45,48] In addition, the K^+ desolvation energy (E_a) in the LHCE is 16.18 kJ mol^{-1}, which is considerably lower compared to the vales observed in the commercial electrolyte (26.86 kJ mol^{-1}), LCE (25.56 kJ mol^{-1}), and HCE (19.04 kJ mol^{-1}) systems. This reduction in E_a can promote the formation of an inorganic-rich SEI, thereby facilitating uniform K deposition chemistry (Figure S10).

The diffusion kinetics of K^+ in the electrolyte plays a crucial role in K deposition behavior, in addition to the robust SEI layer. In commercial electrolyte and LCE, the distribution of K^+ can cause some ions to migrate faster or slower than others, resulting in concentration gradients that can lead to nonuniform K deposition and the formation of K dendrites, as illustrated in Figure 5c,d.[18] Conversely in HCE and LHCE, high or locally high concentrations of K^+ can weaken the concentration gradient, producing a more homogeneous K^+ flux and deposition (Figure 5e,f). As a result, K deposition in HCE and LHCE is more uniform than that in commercial electrolyte and LCE. In addition, the addition of TTE resulted in a decrease in electrolyte viscosity, which allows for a faster transport of K^+. This resulted in the replenishment of K^+ consumed during plating, ultimately producing a denser K deposition in the LHCEs than in the HCE counterpart, as seen in the SEM results. The superior diffusion kinetics of K^+ is also evidenced by the higher transference number of K^+ (t_{K^+}) in the

https://doi.org/10.1021/acsnano.3c06368
ACS Nano 2023, 17, 20325−20333

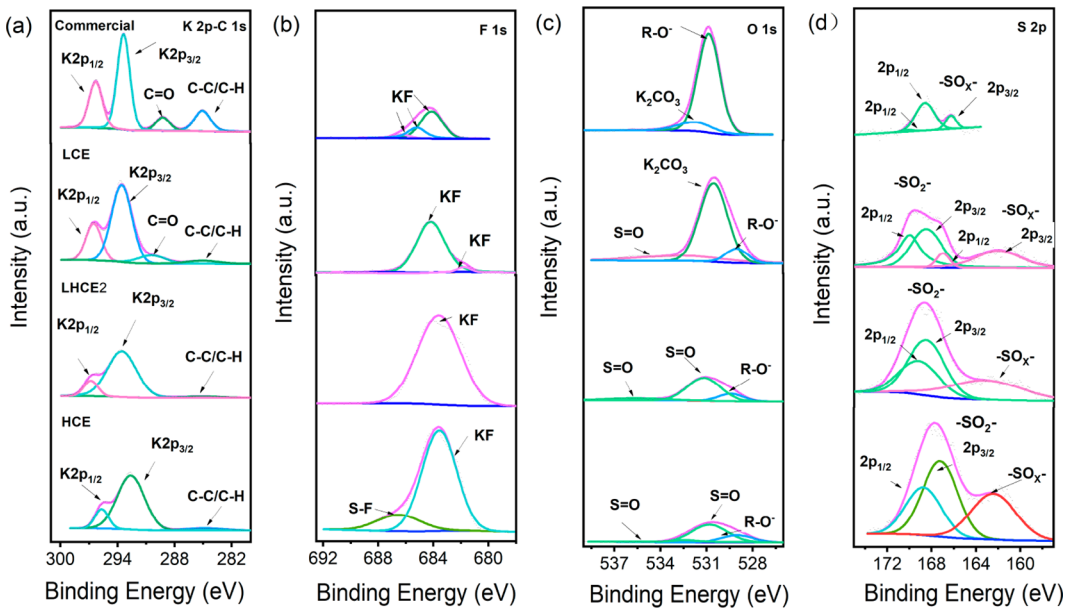

Figure 4. XPS spectra of (a) K 2p and C 1s, (b) F 1s, (c) O 1s, and (d) S 2p peaks of the SEI layer after 20 cycles in K||Cu cells with different electrolytes.

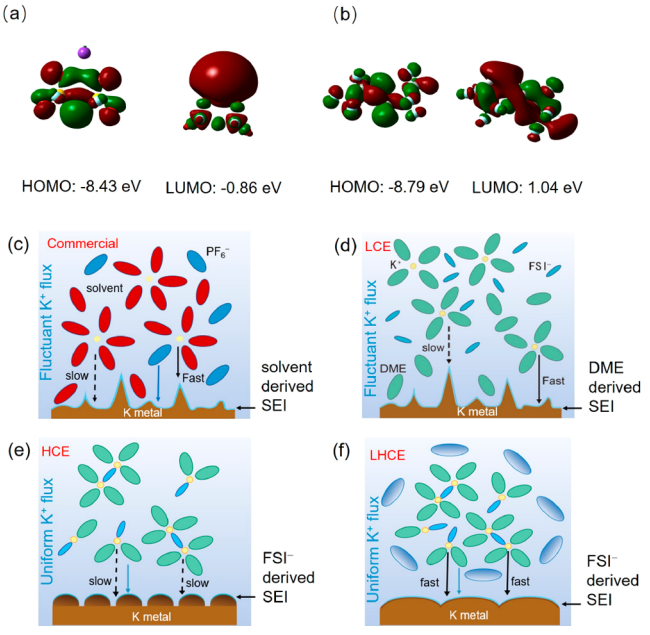

Figure 5. HOMO and LUMO values of (a) KFSI and (b) TTE molecules and schematic diagrams of K plating on Cu electrodes in (c) commercial electrolyte, (d) LCE, (e) HCE, and (f) LHCE.

LHCE (0.47) compared to the HCE (0.25) (Figure S11), which contributes to its excellent rate performance.

Al corrosion is a common phenomenon in traditional electrolytes, especially at high voltages (>4 V). K||Al cells were assembled and kept at 5 V (vs K^+/K) for 20 h to clarify the passivation effect of electrolytes on Al collectors. In LCE, clear evidence of black holes and cracks is clearly observed on the overall surface of the Al foil (Figure S12a), indicating a severe Al corrosion phenomenon, which causes unlimited overcharging. The HCE environment showed slight corrosion due to the high salt content (Figure S12b). However, the Al foil in LHCE2 remained intact and smooth (Figure S12c), indicating good protection provided by TTE. The corrosion of Al foil was also further analyzed using chronoamperometry (CA) profiles, which showed that the corrosion current in LHCE2 was significantly lower than in LCE and HCE. These findings suggest that LHCE2 is compatible with Al collectors and provides good protection against corrosion (Figure S12d). The impressive results obtained in high-voltage PMBs can be attributed to the incorporation of TTE that generates additional AlF_3 passivation layers on the Al collectors.[49] This process effectively inhibits the corrosion of Al, enabling LHCE2 to be applied to high voltage.

To evaluate the practical application of LHCE2 as a safe electrolyte for PMBs, K||$KFe^{II}Fe^{III}(CN)_6$ full cells were assembled using K metal as the anode and $KFe^{II}Fe^{III}(CN)_6$ as the cathode (Figures S13 and S14). The discharge capacity of the K||$KFe^{II}Fe^{III}(CN)_6$ full cells is 67 mAh g^{-1} even after 100 cycles in 100 mAh g^{-1} (based on the mass of $KFe^{II}Fe^{III}(CN)_6$). More importantly, the CE can reach almost 99% in 100 cycles (Figure 6a). Furthermore, the almost overlapping charge−discharge curves with low polarization further demonstrate good reversible chemical behavior (Figure 6b). The rate performance of the K||$KFe^{II}Fe^{III}(CN)_6$ full cells was also investigated (Figure 6c). As the current densities gradually change from 50 to 100, 200, and 500 mA g^{-1}, the full cells can still provide considerable reversible capacities of 81, 73, 70, and 59 mAh g^{-1}, respectively. When the current density is reduced to 50 mA g^{-1}, a reversible capacity of 83 mAh g^{-1} is still obtained. The charge/discharge curves of the full cell at different current densities always display a clear voltage plateau (Figure 6d), corresponding to Fe^{II}/Fe^{III} redox couples, which is further confirmed by cyclic voltammetry (CV) testing (Figure 6e). The above results demonstrate that the LHCE allows the K||$KFe^{II}Fe^{III}(CN)_6$ full cells to obtain good electrochemical performance, which is attributed to the high ionic conductivity and the improved wettability, as well as the uniform CEI formed in LHCE (Figure S15). All of these results clearly confirm that LHCE with TTE as a diluent can be an effective electrolyte strategy for building safe PMBs with high performance.

https://doi.org/10.1021/acsnano.3c06368
ACS Nano 2023, 17, 20325−20333

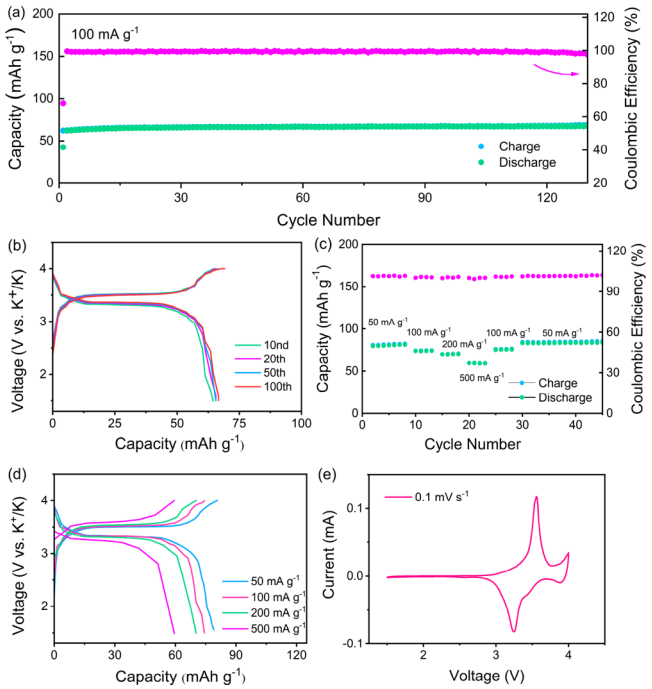

Figure 6. Electrochemical characterizations of K||KFe^{II}Fe^{III}(CN)$_6$ full cells: (a) cycling performance at 100 mA g^{-1}; (b) charge−discharge voltage profiles at different cycles; (c) rate capability; (d) charge−discharge voltage profiles at different current densities from 50 to 500 mA g^{-1}; (e) cyclic voltammetry at 0.1 mV s^{-1}.

CONCLUSION

In summary, a type of LHCE utilizing TTE as an inert diluent was developed, demonstrating great potential for ultrastable PMBs. The LHCE (KFSI/DME/TTE = 1:2:1) allows K||K cells to show excellent reversible plating/stripping performance for up to 2000 h, with an exceptional CE (98%) and no dendrite growth. K||Cu cells with LHCE have exhibited an ultralong cycle life of more than 800 cycles at a current density of 0.1 mA cm^{-2}. The excellent electrochemical performance of the LHCE is attributed to the preservation of the local K$^+$−FSI$^-$−DME solvation structure, as evidenced by the experimental results and DFT simulations, which facilitates the formation of KF-rich SEI layers on the K metal anode, effectively inhibiting the growth of K dendrites and inducing uniform K deposition. Additionally, LHCE has high ionic conductivity, low cost, and good wettability, making it a promising electrolyte for PMBs. The meaningful findings of this work highlight the importance of electrolyte engineering and provide options for building safety and high-performance PMBs.

METHODS

Materials. KFSI (Energy Chemical) was used after drying at 80 °C for 12 h in a vacuum. TTE (TCI, 95%) and DME (Energy Chemical, 99%) were both dried with molecular sieves prior to use. The electrolytes were prepared by mixing KFSI in DME with or without TTE in a glovebox filled with argon. The LCE and HCE consisted of 1 and 4.8 M KFSI/DME, respectively. The commercial electrolyte, consisting of 0.8 M KPF_6 in EC:DEC (1:1 by volume) was purchased from DodoChem Co. Ltd. Salt/solvent mole ratios were mainly used for the concentration notations of the KFSI/DME electrolytes. Molarity was used for the rest of the electrolyte formulations. Potassium ferricyanide(III) ($K_3Fe(CN)_6$, 99.5%) and iron(II) chloride tetrahydrate ($FeCl_2{\cdot}4H_2O$, 98%) were purchased from Beilian (Tianjin) Chemical Co. Commercial Celgard 2400 polypropylene (PP) and glass fiber (GF-F) separators were purchased from Celgard Corporation and Whatman, respectively. Copper (Cu) foil, aluminum (Al) foil, and poly(vinylidene fluoride) (PVDF) were obtained from Kejing Corporation. *N*-Methyl-2-pyrrolidone (NMP, 99.5%) was obtained from Fuchen (Tianjin) Chemical Reagent Co. All cells were assembled in a glovebox (H_2O <0.1 ppm and O_2 <0.1 ppm) with an argon atmosphere.

Preparation of KFe^{II}Fe^{III}(CN)$_6$ Cathode Material. KFe^{II}Fe^{III}(CN)$_6$, a type of Prussian blue, was synthesized by a modified hydrothermal method.[50] First, 1.646 g of $K_3Fe(CN)_6$ was dissolved in 60 mL of deionized water, loaded into an 80 mL reaction vessel, and magnetically stirred at room temperature for 30 min. Then, 0.99 g of $FeCl_2{\cdot}4H_2O$ was added to the solution and stirred for a further 30 min at room temperature. The reaction kettle containing the homogeneously mixed solution was then heated to 80 °C for 24 h. The product was collected by centrifugation at 4000 rpm and washed several times with deionized water and ethanol. After drying under a vacuum at 60 °C for 12 h, the final KFe^{II}Fe^{III}(CN)$_6$ nanoparticles were obtained.

Electrochemical Measurements. Cu foil was cut into circular sheets of 16 mm diameter and pretreated with a 1 M HCl solution to remove oxidized surfaces. Celgard 2400 and GF-F were used as separators. 80 μL of electrolyte was added to each cell. The K||Cu cells consisted of K metal as the counter electrode and Cu foil as the working electrode. The cells were charged to 1 V vs K$^+$/K and discharged to 0.05 and 0.1 mA cm^{-2}. K||K symmetric cells were assembled with K metal as the working electrode and counter electrode, and the cells were tested at 0.05 or 0.1 mA cm^{-2} with a plating−stripping time of 1 h. The desolvation energy (E_a) of K$^+$ in electrolytes was analyzed by EIS data at temperatures ranging from 298 to 323 K according to the Arrhenius formula (eq S1).

$$\sigma = A \exp(-E_a/RT) \quad \text{(S1)}$$

K||KFe^{II}Fe^{III}(CN)$_6$ Full Cells. 70 wt % KFe^{II}Fe^{III}(CN)$_6$, 20 wt % Super-P, and 10 wt % PVDF were homogeneously mixed in NMP. The resulting paste was pasted onto Al foil and then dried under vacuum at 120 °C for 12 h. The effective mass loading of the KFe^{II}Fe^{III}(CN)$_6$ cathode was approximately 0.8−1.0 mg cm^{-2}. K||KFe^{II}Fe^{III}(CN)$_6$ full cells were assembled with K metal as the anode, KFe^{II}Fe^{III}(CN)$_6$ as the cathode, LHCE2 as the electrolyte, and GF-F as the separator. Charge and discharge tests were performed at different current densities in the voltage range of 1.5−4.0 V. Electrochemical tests were carried out on an electrochemical workstation.

Characterizations. The ionic conductivity of the electrolytes was determined by the electrochemical impedance (EIS) method on a German Zanher workstation. The EIS was carried out in the frequency range of 100 mHz to 100 kHz with an alternating-current (AC) signal amplitude of 10 mV. Al corrosion was determined using a VMP-300 instrument. Specifically, LSV testing was performed at a rate of 0.5 mV s^{-1} from open circuit voltage to 5 V (vs K$^+$/K). Then, the voltage was kept at 5 V for about 20 h. After the disassembly of the cell, the Al foil was rinsed with DME. The wettability of the electrolyte on Celgard 2400 was studied by using a contact angle test (JJ2000B2, Powereach, China). The solvation structures of electrolytes were studied by using Raman spectroscopy (VERTEX 70). The circulating electrodes were disassembled in a glovebox filled with argon, cleaned with DME to remove salt residues, and dried in the glovebox. The morphology of the samples was measured by using SEM (Hitachi S-4800) and EDS, respectively. XPS data were collected using Al Kα radiation on a Kratos axis super XPS spectrometer. Samples were cleaned in DME and then transferred to the XPS analysis chamber via a sealed device to prevent exposure to air and water. XRD was recorded with a Rigaku Smart Lab SE diffractometer with a Cu Kα source at the step rate of 2° per minute.

Theoretical Calculations. The partial charges of KFSI and TTE molecules were calculated using Gaussian 16 code, and 6-31+g(d,p) basis functions were applied.[51] The OPLSS-AA force field and MKTOP were used to parametrize all atoms, such as the bond

https://doi.org/10.1021/acsnano.3c06368
ACS Nano 2023, 17, 20325−20333

parameters, angle parameters, dihedral angles, and so on.[52] The solvation structure of K^+ in two different electrolytes (HCE and LHCE) was simulated. The monomer ratio of KFSI/DME/TTE was 1:2:1. 100 KFSI and 200 DME molecules were randomly inserted into a cube box with a side length of 6.0 nm; 100 KFSI, 200 DME, and 100 TTE molecules were randomly inserted into a cube box with a side length of 6.0 nm as well. The molecular dynamics (MD) simulation was performed with the GROMACS 2019 software package.[53−56] The steepest descent method was applied to minimize the initial energy for each system with a force tolerance of 1 kJ mol^{-1} nm^{-1} and a maximum step size of 0.002 ps before MD calculations. In all three directions, periodic boundary conditions were imposed. A leapfrog algorithm was used to integrate the Newtonian equation of motion. Then, a 20 ns production simulation under an NPT ensemble with a time step of 2 fs was carried out for data collection. In NPT simulations, the pressure was maintained at 1 bar by a Berendsen barostat in an isotropic manner.[57] The temperature was maintained by a V-rescale thermostat at 298.15 K. The LINCS algorithm was used to constrain bond lengths of hydrogen atoms. The cutoff distance of nonbonded interactions was 1 nm, and the long-range electrostatic interactions were calculated by the Particle-Mesh-Ewald (PME) method. PME with a fourth-order interpolation was used to evaluate the electrostatic interactions, and the grid spacing was 1.0 Å, whereas a cutoff of 1.0 Å was employed to calculate the short-range van der Waals interactions. After 20 ns of MD simulations, we analyzed the radial distribution function (RDF) and coordination number between K^+ and O atoms in FSI^-, DME, and TTE molecules. The HOMO and LUMO values of KFSI and TTE were calculated with the Gaussian 09 package, and their reduction stability was compared. Density functional theory (DFT) calculations (B3LYP method) were done with the 6-311(d,p) basis set. The conductor-variant polarized continuum model was employed to include the solvent effect. The dielectric constant of DME was 7.3.

ASSOCIATED CONTENT

Supporting Information

The Supporting Information is available free of charge at https://pubs.acs.org/doi/10.1021/acsnano.3c06368.

Materials characterizations, electrochemical performances (voltage−time, Coulombic efficiency, and CV curves of K||Cu cells) and Raman, NMR, SEM, XPS, and EIS characterizations (PDF)

AUTHOR INFORMATION

Corresponding Authors

Xingchao Wang − *State Key Laboratory of Chemistry and Utilization of Carbon Based Energy Resources; Key Laboratory of Advanced Functional Materials, Autonomous Region; Institute of Applied Chemistry, College of Chemistry, Xinjiang University, Urumqi 830046 Xinjiang, People's Republic of China*; orcid.org/0000-0001-7380-9618; Email: xcwang@xju.edu.cn

Aikai Yang − *Forschungszentrum Jülich GmbH, Institute of Energy and Climate Research, Materials Synthesis and Processing (IEK-1), 52425 Jülich, Germany*; Email: aikaiyang@gmail.com

Ying Sun − *Xinjiang Uygur Autonomous Region Product Quality Supervision and Inspection Institute, Key Laboratory of Improvised Explosive Chemicals for State Market Regulation, Urumqi 830011 Xinjiang, People's Republic of China*; Email: ichemabc@126.com

Authors

Ping Gao − *State Key Laboratory of Chemistry and Utilization of Carbon Based Energy Resources; Key Laboratory of Advanced Functional Materials, Autonomous Region; Institute of Applied Chemistry, College of Chemistry, Xinjiang University, Urumqi 830046 Xinjiang, People's Republic of China*

Fei Zhang − *State Key Laboratory of Chemistry and Utilization of Carbon Based Energy Resources; Key Laboratory of Advanced Functional Materials, Autonomous Region; Institute of Applied Chemistry, College of Chemistry, Xinjiang University, Urumqi 830046 Xinjiang, People's Republic of China*

Miaomiao Wu − *State Key Laboratory of Chemistry and Utilization of Carbon Based Energy Resources; Key Laboratory of Advanced Functional Materials, Autonomous Region; Institute of Applied Chemistry, College of Chemistry, Xinjiang University, Urumqi 830046 Xinjiang, People's Republic of China*

Qian Xiang − *State Key Laboratory of Chemistry and Utilization of Carbon Based Energy Resources; Key Laboratory of Advanced Functional Materials, Autonomous Region; Institute of Applied Chemistry, College of Chemistry, Xinjiang University, Urumqi 830046 Xinjiang, People's Republic of China*

Jixi Guo − *State Key Laboratory of Chemistry and Utilization of Carbon Based Energy Resources; Key Laboratory of Advanced Functional Materials, Autonomous Region; Institute of Applied Chemistry, College of Chemistry, Xinjiang University, Urumqi 830046 Xinjiang, People's Republic of China*

Yudai Huang − *State Key Laboratory of Chemistry and Utilization of Carbon Based Energy Resources; Key Laboratory of Advanced Functional Materials, Autonomous Region; Institute of Applied Chemistry, College of Chemistry, Xinjiang University, Urumqi 830046 Xinjiang, People's Republic of China*

Complete contact information is available at: https://pubs.acs.org/10.1021/acsnano.3c06368

Author Contributions

[‖]P.G. and F.Z. contributed equally to this work.

Author Contributions

The manuscript was written through contributions of all authors. All authors have given approval to the final version of the manuscript. P.G. and F.Z. carried out the synthetic experiments and analyses and wrote the paper. X.W., A.Y., and Y.S. conceived the idea and designed the experiments. J.G. and Y.H. supervised the project. M.W. and Q.X. assisted with the experiments. All authors reviewed and commented on the manuscript.

Notes

The authors declare no competing financial interest.

ACKNOWLEDGMENTS

This work was financially supported by the National Natural Science Foundation of China (21905242, 22065033, 21965034, and U1903217), the Nature Science Foundation of Xinjiang Province (2022D01E35, 2022D01A105 and 2022B01024), and the Doctoral Innovation Project of Xinjiang University (XJU2022BS049 and XJU2023BS033).

REFERENCES

(1) Xiong, P.; Han, X.; Zhao, X.; Bai, P.; Liu, Y.; Sun, J.; Xu, Y. Room-Temperature Potassium-Sulfur Batteries Enabled by Micro-

porous Carbon Stabilized Small-Molecule Sulfur Cathodes. *ACS Nano* **2019**, *13*, 2536−2543.
(2) Moon, J.; Kim, D. O.; Bekaert, L.; Song, M.; Chung, J.; Lee, D.; Hubin, A.; Lim, J. Non-Fluorinated Non-Solvating Co-Solvent Enabling Superior Performance of Lithium Metal Negative Electrode Battery. *Nat. Commun.* **2022**, *13*, 4538.
(3) Bird, R.; Baum, Z. J.; Yu, X.; Ma, J. The Regulatory Environment for Lithium-Ion Battery Recycling. *ACS Energy Lett.* **2022**, *7*, 736−740.
(4) Xu, J.; Xu, Y.; Bu, X. H. Advances in Emerging Crystalline Porous Materials. *Small.* **2021**, *17*, No. e2102331.
(5) Yang, J.; Zhao, X.; Yang, J.; Xu, Y.; Li, Y. High-Performance Poly(1-naphthylamine)/Mesoporous Carbon Cathode for Lithium-Ion Batteries with Ultralong Cycle Life of 45000 Cycles at −15 degrees C. *Adv. Sci.* **2023**, *10*, No. e2302490.
(6) Feng, Y.; Zhou, L.; Ma, H.; Wu, Z.; Zhao, Q.; Li, H.; Zhang, K.; Chen, J. Challenges and advances in wide-temperature rechargeable lithium batteries. *Energy Environ. Sci.* **2022**, *15*, 1711−1759.
(7) Zhou, M.; Bai, P.; Ji, X.; Yang, J.; Wang, C.; Xu, Y. Electrolytes and Interphases in Potassium Ion Batteries. *Adv. Mater.* **2021**, *33*, No. e2003741.
(8) Kim, J.; Kim, Y.; Yoo, J.; Kwon, G.; Ko, Y.; Kang, K. Organic Batteries for a Greener Rechargeable World. *Nat. Rev. Mater.* **2023**, *8*, 54−70.
(9) Guo, Y.; Wu, S.; He, Y.-B.; Kang, F.; Chen, L.; Li, H.; Yang, Q.-H. Solid-State Lithium Batteries: Safety and Prospects. *eScience.* **2022**, *2*, 138−163.
(10) Zhang, H.; Huang, L.; Xu, H.; Zhang, X.; Chen, Z.; Gao, C.; Lu, C.; Liu, Z.; Jiang, M.; Cui, G. A Polymer Electrolyte with a Thermally Induced Interfacial Ion-Blocking Function Enables Safety-Enhanced Lithium Metal Batteries. *eScience.* **2022**, *2*, 201−208.
(11) Sun, L.; Liu, Y.; Shao, R.; Wu, J.; Jiang, R.; Jin, Z. Recent Progress and Future Perspective on Practical Silicon Anode-Based Lithium Ion Batteries. *Energy Stor. Mater.* **2022**, *46*, 482−502.
(12) Shi, Y.; Yang, J.; Yang, J.; Wang, Z.; Chen, Z.; Xu, Y. Quinone-Amine Polymer Nanoparticles Prepared through Facile Precipitation Polymerization as Ultrafast and Ultralong Cycle Life Cathode Materials for Lithium-Ion Batteries. *Adv. Funct. Mater.* **2022**, *32*, 2111307.
(13) Xiong, P.; Wu, J.; Zhou, M.; Xu, Y. Bismuth−Antimony Alloy Nanoparticle@Porous Carbon Nanosheet Composite Anode for High-Performance Potassium-Ion Batteries. *ACS Nano* **2020**, *14*, 1018−1026.
(14) Jian, Z.; Luo, W.; Ji, X. Carbon Electrodes for K-Ion Batteries. *J. Am. Chem. Soc.* **2015**, *137*, 11566−11569.
(15) Wang, Z.; Dong, K.; Wang, D.; Luo, S.; Liu, Y.; Wang, Q.; Zhang, Y.; Hao, A.; Shi, C.; Zhao, N. A Nanosized Snsb Alloy Confined in N-Doped 3d Porous Carbon Coupled with Ether-Based Electrolytes toward High-Performance Potassium-Ion Batteries†. *J. Mater. Chem. A* **2019**, *7*, 14309−14318.
(16) Xie, K.; Yuan, K.; Li, X.; Lu, W.; Shen, C.; Liang, C.; Vajtai, R.; Ajayan, P.; Wei, B. Superior Potassium Ion Storage via Vertical MoS2 "Nano-Rose" with Expanded Interlayers on Graphene. *Small.* **2017**, *13*, 1701471.
(17) Lei, K.; Li, F.; Mu, C.; Wang, J.; Zhao, Q.; Chen, C.; Chen, J. High K-Storage Performance Based on The Synergy of Dipotassium Terephthalate and Ether-Based Electrolytes†. *Energy Environ. Sci.* **2017**, *10*, 552−557.
(18) Wang, H.; Hu, J.; Dong, J.; Lau, K. C.; Qin, L.; Lei, Y.; Li, B.; Zhai, D.; Wu, Y.; Kang, F. Artificial Solid-Electrolyte Interphase Enabled High-Capacity and Stable Cycling Potassium Metal Batteries. *Adv. Energy Mater.* **2019**, *9*, 1902697.
(19) Hu, Y.; Fan, L.; Rao, A. M.; Yu, W.; Zhuoma, C.; Feng, Y.; Qin, Z.; Zhou, J.; Lu, B. Cyclic-Anion Salt for High-Voltage Stable Potassium-Metal Batteries. *Natl. Sci. Rev.* **2022**, *9* (9), No. nwac134.
(20) Zhang, X.; Cheng, X.; Xiang, C.; Chong, Y.; Zhang, Q. Fluoroethylene Carbonate Additives to Render Uniform Li Deposits in Lithium Metal Batteries. *Adv. Funct. Mater.* **2017**, *27*, 1605989.
(21) Ni, L.; Xu, G.; Li, C.; Cui, G. Electrolyte Formulation Strategies for Potassium-Based Batteries. *Exploration.* **2022**, *2*, 20210239.
(22) Zhou, X.; Zhang, Q.; Zhu, Z.; Cai, Y.; Li, H.; Li, F. Anion Reinforced Solvation for Gradient Inorganic-Rich Interphase Enables High-Rate and Stable Sodium Batteries. *Angew. Chem., Int. Ed.* **2022**, *61*, No. e202205045.
(23) Zhou, Q.; Dong, S.; Lv, Z.; Xu, G.; Huang, L.; Wang, Q.; Cui, Z.; Cui, G. A Temperature-Responsive Electrolyte Endowing Superior Safety Characteristic of Lithium Metal Batteries. *Adv. Energy Mater.* **2020**, *10*, 1903441.
(24) Cheng, H.; Sun, Q.; Li, L.; Zou, Y.; Wang, Y.; Cai, T.; Zhao, F.; Liu, G.; Ma, Z.; Wahyudi, W.; Li, Q.; Ming, J. Emerging Era of Electrolyte Solvation Structure and Interfacial Model in Batteries. *ACS Energy Lett.* **2022**, *7*, 490−513.
(25) Hu, X.; Li, Y.; Liu, J.; Wang, Z.; Bai, Y.; Ma, J. Constructing LiF/Li2CO3-rich heterostructured electrode electrolyte interphases by electrolyte additive for 4.5 V well-cycled lithium metal batteries. *Science Bulletin.* **2023**, *68*, 1295−1305.
(26) Xiao, N.; Zheng, J.; Gourdin, G.; Schkeryantz, L.; Wu, Y. Anchoring an Artificial Protective Layer To Stabilize Potassium Metal Anode in Rechargeable K-O2 Batteries. *ACS Appl. Mater. Interfaces* **2019**, *11*, 16571−16577.
(27) Tang, X.; Zhou, D.; Li, P.; Guo, X.; Sun, B.; Liu, H.; Yan, K.; Gogotsi, Y.; Wang, G. MXene-Based Dendrite-Free Potassium Metal Batteries. *Adv. Mater.* **2020**, *32*, 1906739.
(28) Zhao, Y.; Liu, B.; Yi, Y.; Lian, X.; Wang, M.; Li, S.; Yang, X.; Sun, J. An Anode-Free Potassium-Metal Battery Enabled by a Directly Grown Graphene-Modulated Aluminum Current Collector. *Adv. Mater.* **2022**, *34*, No. e2202902.
(29) Li, S.; Zhu, H.; Liu, Y.; Han, Z.; Peng, L.; Li, S.; Yu, C.; Cheng, S.; Xie, J. Codoped Porous Carbon Nanofibres as a Potassium Metal Host for Nonaqueous K-Ion Batteries. *Nat. Commun.* **2022**, *13*, 4911.
(30) Xiao, K.; Wu, J.-F.; Yan, H.; Mo, Y.; Zhou, W.; Peng, Y.; Chen, S.; Cui, X.; Chen, L.; Xu, C.; Liu, J. Intercalation-Deposition Mechanism Induced by Aligned Carbon Fiber toward Dendrite-Free Metallic Potassium Batteries. *Energy Stor. Mater.* **2022**, *51*, 122−129.
(31) Chen, J.; Yu, D.; Zhu, Q.; Liu, X.; Wang, J.; Chen, W.; Ji, R.; Qiu, K.; Guo, L.; Wang, H. Low-Temperature High-Areal-Capacity Rechargeable Potassium-Metal Batteries. *Adv. Mater.* **2022**, *34*, No. e2205678.
(32) Park, J.; Jeong, Y.; Alfaruqi, M. H.; Liu, Y.; Xu, X.; Xiong, S.; Jung, M.-G.; Jung, H.-G.; Kim, J.; Hwang, J.-Y.; Sun, Y.-K. Stable Solid Electrolyte Interphase for Long-Life Potassium Metal Batteries. *ACS Energy Lett.* **2022**, *7*, 401−409.
(33) Qiu, B.; Xu, F.; Qiu, J.; Yang, M.; Zhang, G.; He, C.; Zhang, P.; Mi, H.; Ma, J. Electrode-electrolyte interface mediation via molecular anchoring for 4.7 V quasi-solid-state lithium metal batteries. *Energy Stor. Mater.* **2023**, *60*, 102832.
(34) Zheng, J.; Chen, S.; Zhao, W.; Song, J.; Engelhard, M. H.; Zhang, J.-G. Extremely Stable Sodium Metal Batteries Enabled by Localized High-Concentration Electrolytes. *ACS Energy Lett.* **2018**, *3*, 315−321.
(35) Yu, Z.; Balsara, N. P.; Borodin, O.; Gewirth, A. A.; Hahn, N. T.; Maginn, E. J.; Persson, K. A.; Srinivasan, V.; Toney, M. F.; Xu, K.; Zavadil, K. R.; Curtiss, L. A.; Cheng, L. Beyond Local Solvation Structure: Nanometric Aggregates in Battery Electrolytes and Their Effect on Electrolyte Properties. *ACS Energy Lett.* **2022**, *7*, 461−470.
(36) Giffin, G. A. The Role of Concentration in Electrolyte Solutions for Non-Aqueous Lithium-Based Batteries. *Nat. Commun.* **2022**, *13*, 5250.
(37) Qi, S.; Tang, X.; He, J.; Liu, J.; Ma, J. Construction of Localized High-Concentration PF6− Region for Suppressing NCM622 Cathode Failure at High Voltage. *Small Methods.* **2023**, *7*, 2201693.
(38) Doi, T.; Shimizu, Y.; Hashinokuchi, M.; Inaba, M. Dilution of Highly Concentrated LiBF4/Propylene Carbonate Electrolyte Solution with Fluoroalkyl Ethers for 5-V LiNi0.5Mn1.5O4 Positive Electrodes. *J. Electrochem. Soc.* **2017**, *164*, A6412−A6416.
(39) Chen, S.; Zheng, J.; Mei, D.; Han, K. S.; Engelhard, M. H.; Zhao, W.; Xu, W.; Liu, J.; Zhang, J. G. High-Voltage Lithium-Metal

Batteries Enabled by Localized High-Concentration Electrolytes. *Adv. Mater.* **2018**, *30*, No. e1706102.
(40) Piao, N.; Ji, X.; Xu, H.; Fan, X.; Chen, L.; Liu, S.; Garaga, M. N.; Greenbaum, S. G.; Wang, L.; Wang, C.; He, X. Countersolvent Electrolytes for Lithium-Metal Batteries. *Adv. Energy Mater.* **2020**, *10*, 1903568.
(41) Zhang, S.; Li, S.; Lu, Y. Designing Safer Lithium-Based Batteries with Nonflammable Electrolytes: a Review. *eScience* **2021**, *1*, 163−177.
(42) Wang, H.; Yu, D.; Wang, X.; Niu, Z.; Chen, M.; Cheng, L.; Zhou, W.; Guo, L. Electrolyte Chemistry Enables Simultaneous Stabilization of Potassium Metal and Alloying Anode for Potassium-Ion Batteries. *Angew.Chem.Int.Ed.* **2019**, *58*, 16451−16455.
(43) Xiao, N.; McCulloch, W. D.; Wu, Y. Reversible Dendrite-Free Potassium Plating and Stripping Electrochemistry for Potassium Secondary Batteries. *J. Am. Chem. Soc.* **2017**, *139*, 9475−9478.
(44) Ren, X.; He, M.; Xiao, N.; McCulloch, W. D.; Wu, Y. Greatly Enhanced Anode Stability in K-Oxygen Batteries with an In Situ Formed Solvent- and Oxygen-Impermeable Protection Layer. *Adv. Energy Mater.* **2017**, *7*, 1601080.
(45) Xu, W.; Wang, H.; Hu, J.; Zhang, H.; Zhang, B.; Kang, F.; Zhai, D. A highly concentrated electrolyte for high-efficiency potassium metal batteries. *Chem. Commun.* **2021**, *57*, 1034−1037.
(46) Girard, G. M. A.; Hilder, M.; Dupre, N.; Guyomard, D.; Nucciarone, D.; Whitbread, K.; Zavorine, S.; Moser, M.; Forsyth, M.; MacFarlane, D. R.; Howlett, P. C. Spectroscopic Characterization of the SEI Layer Formed on Lithium Metal Electrodes in Phosphonium Bis(fluorosulfonyl)imide Ionic Liquid Electrolytes. *ACS Appl. Mater. Interfaces.* **2018**, *10*, 6719−6729.
(47) Yao, Y. X.; Chen, X.; Yan, C.; Zhang, X. Q.; Cai, W. L.; Huang, J. Q.; Zhang, Q. Regulating Interfacial Chemistry in Lithium-Ion Batteries by a Weakly Solvating Electrolyte*. *Angew.Chem.Int.Ed.* **2021**, *60*, 4090−4097.
(48) Zheng, J.; Lochala, J. A.; Kwok, A.; Deng, Z. D.; Xiao, J. Research Progress towards Understanding the Unique Interfaces between Concentrated Electrolytes and Electrodes for Energy Storage Applications. *Adv. Sci.* **2017**, *4*, 1700032.
(49) Ren, X.; Chen, S.; Lee, H.; Mei, D.; Engelhard, M. H.; Burton, S. D.; Zhao, W.; Zheng, J.; Li, Q.; Ding, M. S.; Schroeder, M.; Alvarado, J.; Xu, K.; Meng, Y. S.; Liu, J.; Zhang, J.-G.; Xu, W. Localized High-Concentration Sulfone Electrolytes for High-Efficiency Lithium-Metal Batteries. *Chem.* **2018**, *4*, 1877−1892.
(50) Liu, P.; Hao, H.; Celio, H.; Cui, J.; Ren, M.; Wang, Y.; Dong, H.; Chowdhury, A. R.; Hutter, T.; Perras, F. A.; Nanda, J.; Watt, J.; Mitlin, D. Multifunctional Separator Allows Stable Cycling of Potassium Metal Anodes and of Potassium Metal Batteries. *Adv. Mater.* **2022**, *34* (7), No. e2105855.
(51) Curtiss, L. A.; Redfern, P. C.; Raghavachari, K. Gaussian-4 Theory. *J. Chem. Phys.* **2007**, *126* (8), No. 084108.
(52) Jorgensen, W. L.; Maxwell, D. S.; Tirado-Rives, J. Development and Testing of the OPLS All-Atom Force Field on Conformational Energetics and Properties of Organic Liquids. *J. Am. Chem. Soc.* **1996**, *118*, 11225−11236.
(53) Van Der Spoel, D.; Lindahl, E.; Hess, B.; Groenhof, G.; Mark, A. E.; Berendsen, H. J. GROMACS: Fast, Flexible, and Free. *J. Comput. Chem.* **2005**, *26* (16), 1701−18.
(54) Abraham, M. J.; Murtola, T.; Schulz, R.; Páll, S.; Smith, J. C.; Hess, B.; Lindahl, E. GROMACS: High Performance Molecular Simulations through Multi-Level Parallelism from Laptops to Supercomputers. *SoftwareX* **2015**, *1-2*, 19−25.
(55) Pronk, S.; Pall, S.; Schulz, R.; Larsson, P.; Bjelkmar, P.; Apostolov, R.; Shirts, M. R.; Smith, J. C.; Kasson, P. M.; van der Spoel, D.; Hess, B.; Lindahl, E. GROMACS 4.5: a High-Throughput and Highly Parallel Open Source Molecular Simulation Toolkit. *Bioinformatics* **2013**, *29* (7), 845−54.
(56) Hess, B.; Kutzner, C.; van der Spoel, D.; Lindahl, E. GROMACS 4: Algorithms for Highly Efficient, Load-Balanced, and Scalable Molecular Simulation. *J. Chem. Theory Comput.* **2008**, *4*, 435−447.
(57) Eslami, H.; Mojahedi, F.; Moghadasi, J. Molecular Dynamics Simulation with Weak Coupling to Heat and Material Baths. *J. Chem. Phys.* **2010**, *133* (8), No. 084105.

https://doi.org/10.1021/acsnano.3c06368
ACS Nano 2023, 17, 20325−20333